Mon. Not. R. astr. Soc. (1980) **190**, 833–851

The structure of Tycho's supernova remnant

S. Nigel Henbest* *Mullard Radio Astronomy Observatory, Cavendish Laboratory, Madingley Road, Cambridge CB3 0HE*

Received 1979 August 13; in original form 1979 July 20

Summary. A map of Tycho's supernova remnant (3C 10) at 2.7 GHz with a resolution of 12×13 arcsec is presented. The remnant shows irregularities down to a scale < 0.1 pc, and is expanding into an inhomogeneous medium having a number density $0.2 \pm 0.1\,\mathrm{cm}^{-3}$ to the SW, and about $0.1\,\mathrm{cm}^{-3}$ to the NE where there are also discrete clouds at least an order of magnitude denser. The geometrical centre (position of SN 1572) is $00^{h}\,22^{m}\,28^{s}.9 \pm 0^{s}.7$, $+63^{\circ}\,51'\,27'' \pm 5''$. The outer edge of the radio remnant marks the shock front, and the emissivity profile requires either (a) adiabatic (Sedov) expansion with a uniform distribution of relativistic electrons, or (b) isothermal expansion with relativistic electron density varying as the thermal plasma density: in either case energy arguments show that the interstellar magnetic field is amplified by an order of magnitude over the expected post-shock value. The radio spectral index is constant (to within 0.2) over the remnant, in the frequency range 0.4–15 GHz.

1 Introduction

Although many maps of the radio structure of Tycho's supernova remnant (3C 10) have been published, observations with a single dish (e.g. Dickel 1969; Klein *et al.* 1979) have insufficient resolving power to reveal details of the 8 arcmin diameter source, while maps made with aperture synthesis instruments (e.g. Hermann & Dickel 1973, 8×11 arcsec; Duin & Strom 1975, 7 arcsec) tend to suffer from undersampling of the aperture plane, and consequent distortions of the large-scale structure. This paper reports on observations of 3C 10 with the Cambridge One-Mile Telescope (OMT) at 2.7 GHz, in which the aperture plane was fully sampled and from which a map with resolution 12×13 arcsec was produced.

The observations are described in Section 2, and compared with previously published maps in Section 3. The high-resolution map is analysed in detail in Section 4. Several different regions are distinguished on the basis of radio and optical morphology, and radio polarization properties, and the physical conditions in each are discussed. The distance to Tycho's supernova remnant has been taken as 4.0 kpc (see Appendix).

* Present address: 210 Priests Lane, Brentwood, Essex.

2 Observations

3C 10 was observed with the OMT (Elsmore, Kenderdine & Ryle 1966) at 2.697 GHz between 1972 September and 1973 January. A full synthesis of 128 spacings (spacing increment 11.7 m) was made, with the exception of the first spacing (11.7 m) which is physically unattainable. The information content of this spacing was inserted into the Fourier transform, however, in the following way. At low spatial frequencies the source appears circularly symmetric, and its visibility function (Fig. 1) approximates closely to that of an infinitesimally thin shell. Since the amplitude at zero spatial frequency is equal to the total flux density (taken from Kellermann, Pauliny-Toth & Williams 1969), the theoretical visibility function is tightly constrained, and the amplitude at spacing one can be interpolated with sufficient accuracy for all position angles of the baseline. (The phase for the first spacing is, to sufficient accuracy, zero since the radio centroid ($00^h\,22^m\,34^s.4$, $+63°\,51'\,48''$; Rosenberg 1972) was chosen as the map centre.)

Simultaneous observations were made at 5 GHz, but these suffered both from undersampling and from a system noise high enough to prevent useful information from being obtained at the longest baselines. Data corresponding to a spacing of 11.7 m were included in the synthesis by scaling the 2.7-GHz visibility function (Fig. 1) and, although the undersampling is worse than at 2.7 GHz, the intensities of the small-scale features around the rim of the remnant are not significantly affected. At 5 GHz, allowance must be made for the shape of the primary beam, a correction amounting to 10 per cent at the rim. (At 2.7 GHz it is < 3 per cent, and no correction was made.)

The primary feeds were rotated during the observations, so that various combinations of the Stokes parameters could be sampled. The final maps correspond to total intensity I.

3 Results

3.1 THE FULL-RESOLUTION MAP AT 2.7 GHz

The full resolution (12.0 × 13.4 arcsec) map at 2.7 GHz is shown in Fig. 2. As far as the small-scale structure is concerned, it is consistent with the 5-GHz map by Duin & Strom

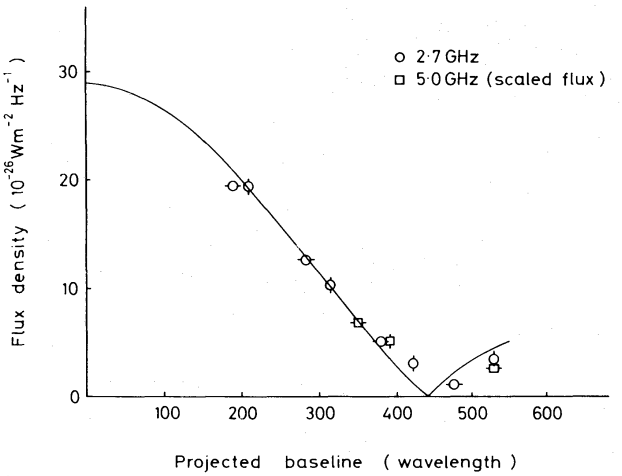

Figure 1. The visibility function of 3C 10 at short baselines. For each interferometer spacing the visibility is shown at orthogonal position angles of the baseline, as indicated by the short bars. The solid line is the theoretical visibility function of an infinitesimally thin shell, fitted to the 2.7-GHz observations and the zero-spacing (total) flux density given by Kellermann *et al.* (1969). The 5-GHz flux densities have been scaled up by a factor of 1.40, appropriate to a spectral index of 0.55 (Kellermann *et al.* 1969).

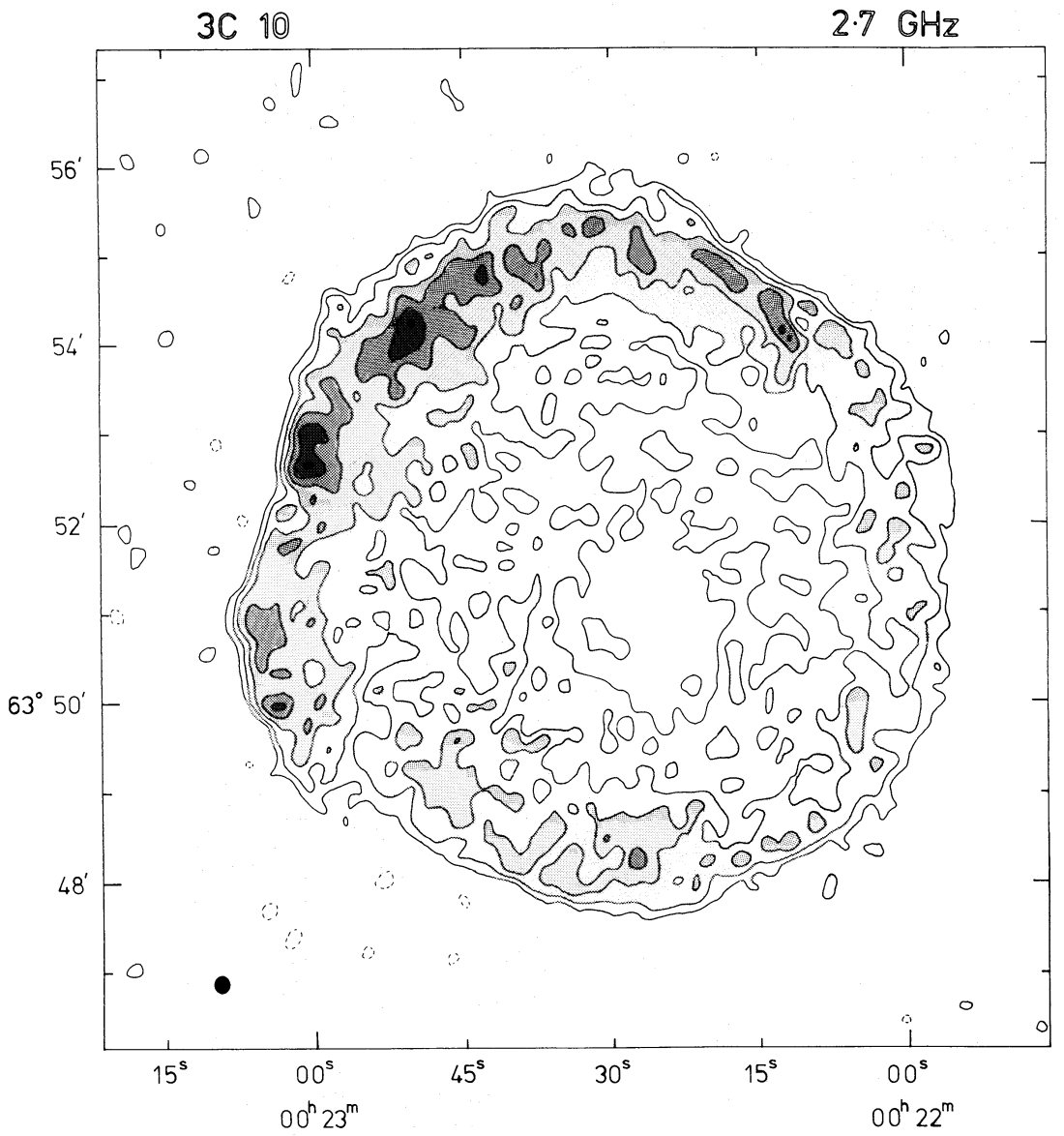

Figure 2. 3C 10 at 2.7 GHz with a resolution of 12.0 × 13.4 arcsec. The beam is shown in the lower left corner. The contours are main-beam brightness temperatures, and contour interval is 11.6 K; the shading obviates any ambiguity between isolated maxima and minima. The zero contour is not shown on this map, and negative contours due to noise temperature of 3.2 K are shown dashed.

(1975) at 7 arcsec resolution; many of the peaks around the shell, and the outer edge of the shell itself, are unresolved even with their smaller beam. Both maps reveal 'breaks' in the shell, where the intensity drops to much less than the mean value around the annulus, and it is evident that an analysis in terms of a smooth shell of emission with superimposed peaks (as attempted by Strom & Duin 1973) is inappropriate for this remnant. There are, however, significant differences in the large-scale structure; the present map should represent this more faithfully because of the fuller sampling of the aperture plane (Section 3.2).

3.2 SPECTRAL INDEX DISTRIBUTION

When smoothed to a resolution of 23 × 27 arcsec (Fig. 3), the present 2.7- and 5-GHz maps are not significantly different from the OMT map at 1.4 GHz (Baldwin 1967; Rosenberg 1972). In the frequency range 1.4–5 GHz there is no significant change in spectral index

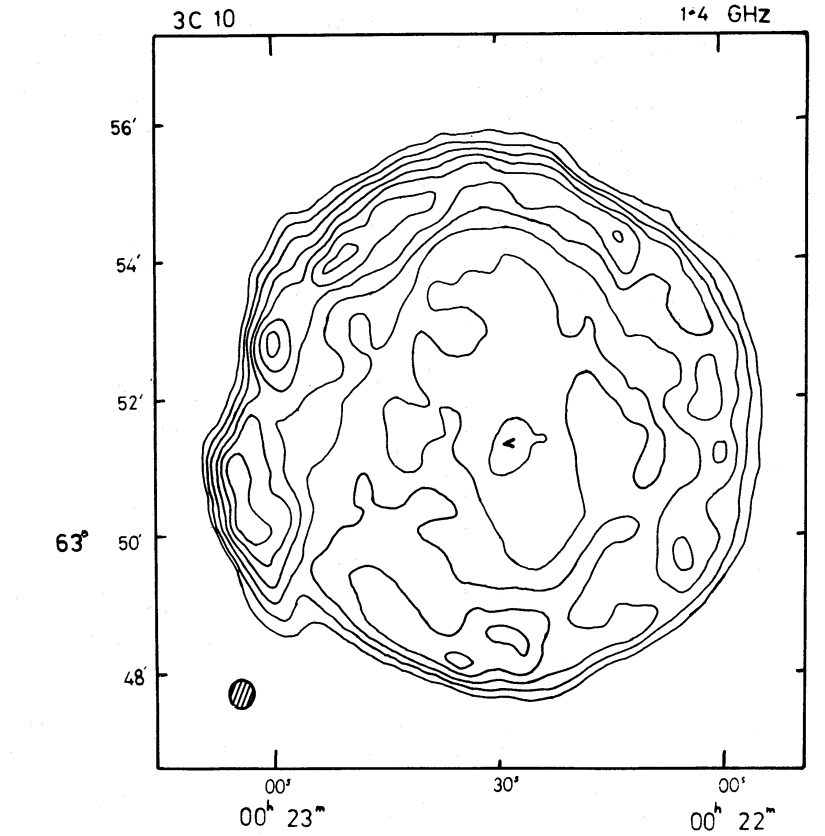

(a)

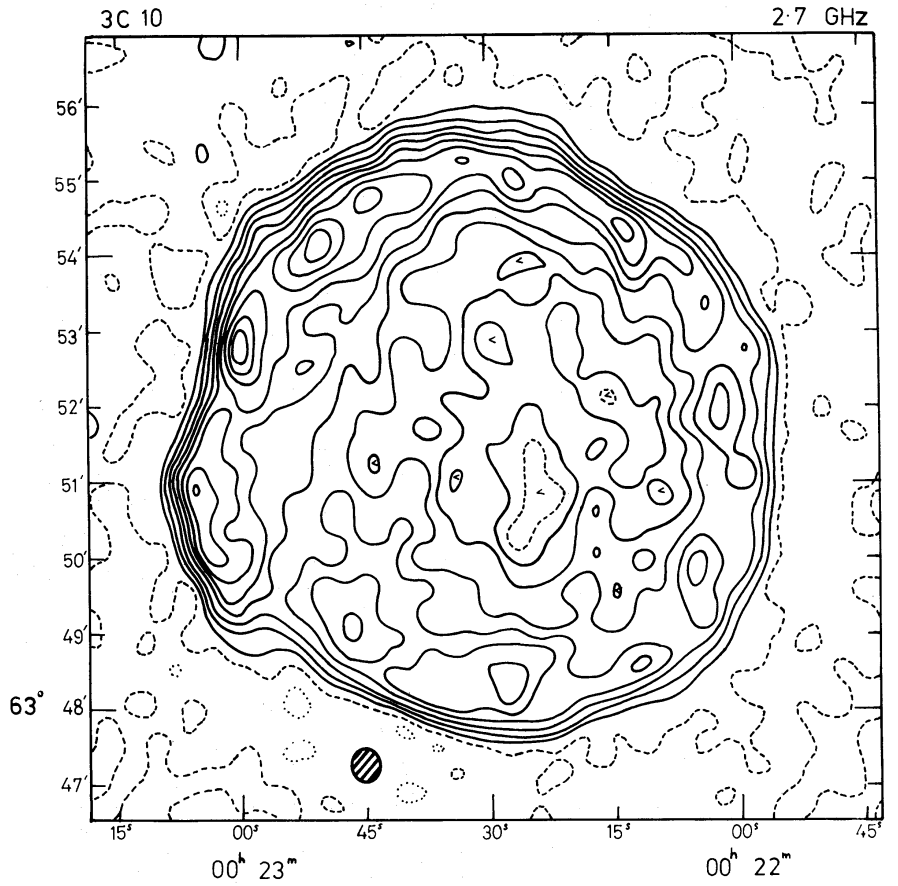

(b)

Figure 3. Maps of 3C 10 at (a) 1.4 (from Rosenberg 1972), (b) 2.7 and (c) 5 GHz, all with a resolution of 24 × 27 arcsec. The contours are main-beam brightness temperatures, with contour intervals 54, 7.6 and 3.0 K respectively: isolated minima are marked <, and the beamsize is shown by the shaded ellipse. The zero contour is not shown on the 1.4-GHz map; on the others it is dashed, with negative contours dotted.

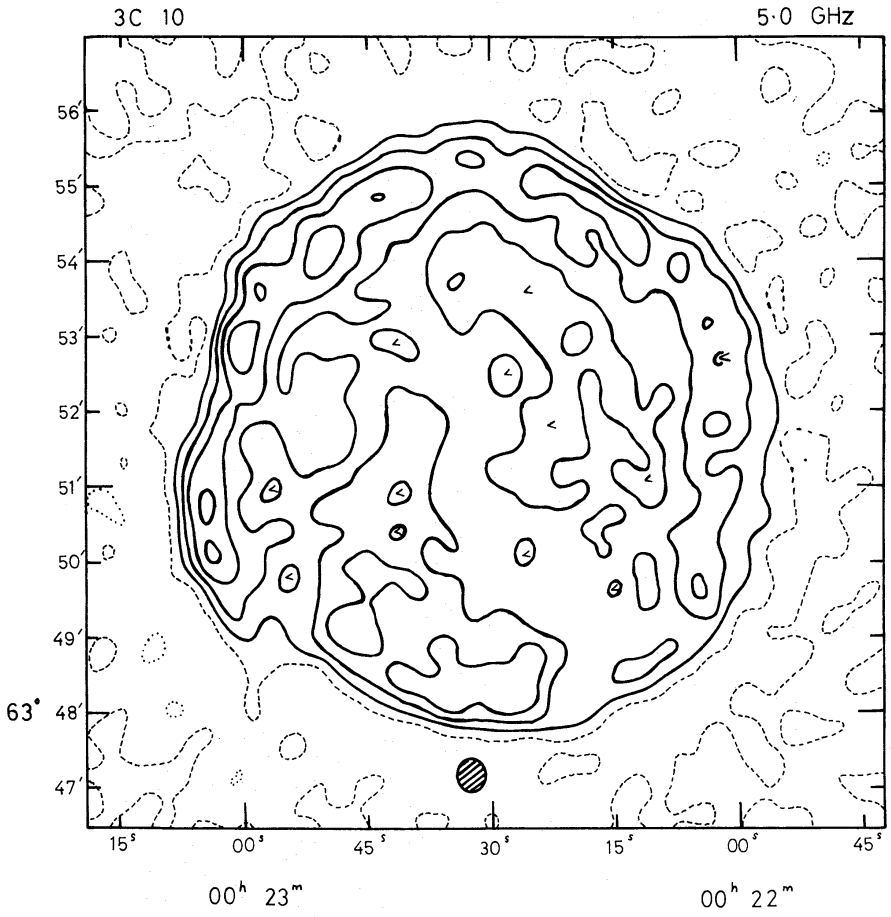

(c)

around the rim (< 0.1 for NE arc, < 0.2 for the fainter SW arc). A similar result has been found for lower frequencies (0.4–1.4 GHz, Rosenberg 1972; 0.6–1.4 GHz, Duin & Strom 1975), so this constancy of spectral index holds over the whole range 0.4–5 GHz.

Weiler & Seielstad (1971) have reported a possible variation in spectral index across 3C 10, between 1.4 and 2.9 GHz, in the sense that the spectrum is flatter at the N and S of the remnant. This variation is not confirmed by the present observations, and it seems that their apparent change in spectral index was due to the undersampling in their observations, which produced a N–S 'grating-ring' response with a radius approximately equal to the diameter of the source.

The mean profile at 2.7 GHz is closely similar to the OMT 1.4-GHz profile, which is itself very similar to the OMT 0.4-GHz profile when smoothed to the same resolution (Fig. 4). The difference in spectral index between the centre and rim is less than 0.1 over the frequency range 0.4–2.7 GHz.

Duin & Strom (1975), however, from a comparison of maps at 0.6 and 1.4 GHz, find the spectrum of the centre to be considerably steeper than that of the rim, 1.0 ± 0.1 and 0.7 ± 0.05 respectively (with spectral index α defined by $S_\nu \propto \nu^{-\alpha}$). Their 1.4-GHz profile, derived from a map made with the Westerbork Synthesis Radio Telescope (WSRT), also differs significantly from that derived from the OMT map at the same frequency, a difference that Strom & Duin (1973) suggest may arise from undersampling in the OMT observations. To investigate this possibility, all the relevant E–W Earth-rotation synthesis observations of 3C 10 have been summarized in Table 1. It can be seen that the best-sampled maps are those from the OMT at 0.4 GHz (Rosenberg 1972) and 2.7 GHz (present observations).

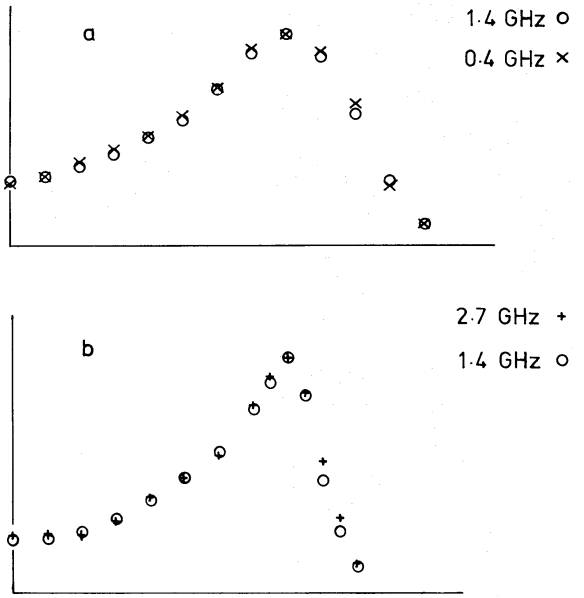

Figure 4. Radial profiles of 3C 10, each the average of eight equally-spaced radial cuts whose abscissae have been scaled to bring the peaks into coincidence. In each comparison the profiles have been normalized to the same maximum intensity: (a) from maps at 0.4 and 1.4 GHz with a resolution of 80 × 90 arcsec; (b) from maps at 1.4 and 2.7 GHz with a resolution of 24 × 27 arcsec.

Table 1. E–W Earth-rotation synthesis maps of 3C 10.

Frequency (GHz)	Baseline increment (m)	(λ)	Instrument*	Reference
0.4	47	64.5	OMT	Rosenberg 1972
0.6	72	144	WSRT	Duin & Strom 1975
1.4	47	224	OMT	Rosenberg 1972
1.4	36	172	WSRT	Strom & Duin 1973
2.7	11.7	106	OMT	Present work
5.0	11.7	195	OMT	Present work
5.0	18	300	WSRT	Duin & Strom 1975

* OMT = Cambridge One-Mile Telescope

WSRT = Westerbork Synthesis Radio Telescope

The agreement between these and the OMT 1.4-GHz map indicates there is no significant distortion in the latter; and it is these maps, covering a wider frequency range than those considered by Duin & Strom, and with a better aperture-plane coverage, which show a negligible change in spectral index from centre to rim.

Maps made with large single-dish radio telescopes at higher frequencies confirm this conclusion. Profiles from the available 15-GHz (Dickel 1969) and 10.7-GHz (Emerson, Klein & Haslam 1979) maps are closely similar to the OMT profile convolved to the same resolution (Fig. 5). The spectrum of the rim appears to be slightly steeper than that of the centre – a difference in the opposite sense from Duin & Strom's result – and even this

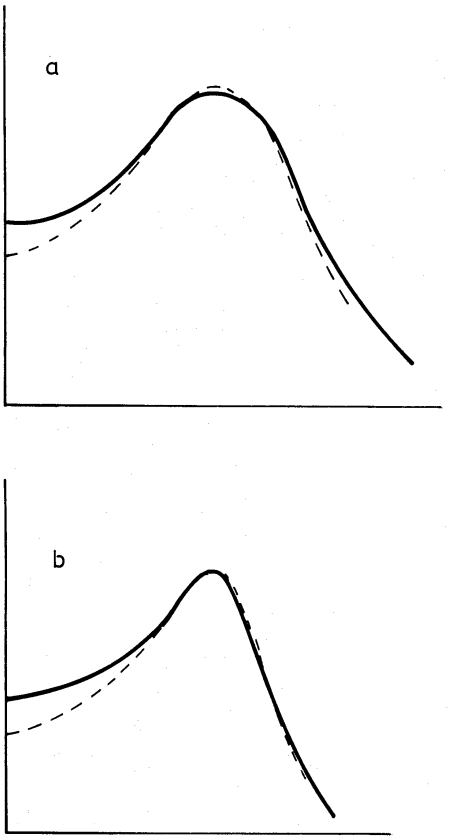

Figure 5. Mean radial profiles at 15 and 10.7 GHz (solid), compared to the OMT 2.7-GHz profile (dashed) from maps convolved to the same resolution: (a) NRAO 43-m telescope, 15 GHz, 123-arcsec beam (Dickel 1969); and (b) Effelsberg 100-m telescope, 10.7 GHz, 70-arcsec beam (Emerson, Klein & Haslam 1979).

small variation (about 0.1 in spectral index) is probably not significant, since the centres of ring-shaped sources are particularly sensitive to distortions of the beamshape when the telescope beamwidth is comparable to the source radius.

After this work was completed, Klein *et al.* (1979) published a comparison between a single-dish 10.7-GHz map of 3C 10 obtained with Effelsberg 100-m telescope and the Westerbork 0.6-GHz map, and reached similar conclusion: they set an upper limit of 0.05 on any difference in spectral index between centre and rim.

4 Discussion

4.1 COMPARISON OF OPTICAL AND RADIO FEATURES

At the resolution of Fig. 2, the outline of the remnant is significantly non-circular: although the impression is of an irregular polygon, the overall shape is well-fitted by two circular arcs (Section 4.3). The rather flatter stretches presumably result from the slower passage of the shock front through regions of higher-than-average interstellar density, a conclusion confirmed for the major straight stretch (in the E) by a study of the radio depolarization (Section 4.2). The brightest and narrowest optical filaments are also found here and at a shorter straight stretch in the NW, and these lie along the outer edge of the radio emission (Fig. 6). The more diffuse optical filaments lie between these regions, superimposed on the radio structure. This is the configuration expected of the optical emission of Tycho's SNR

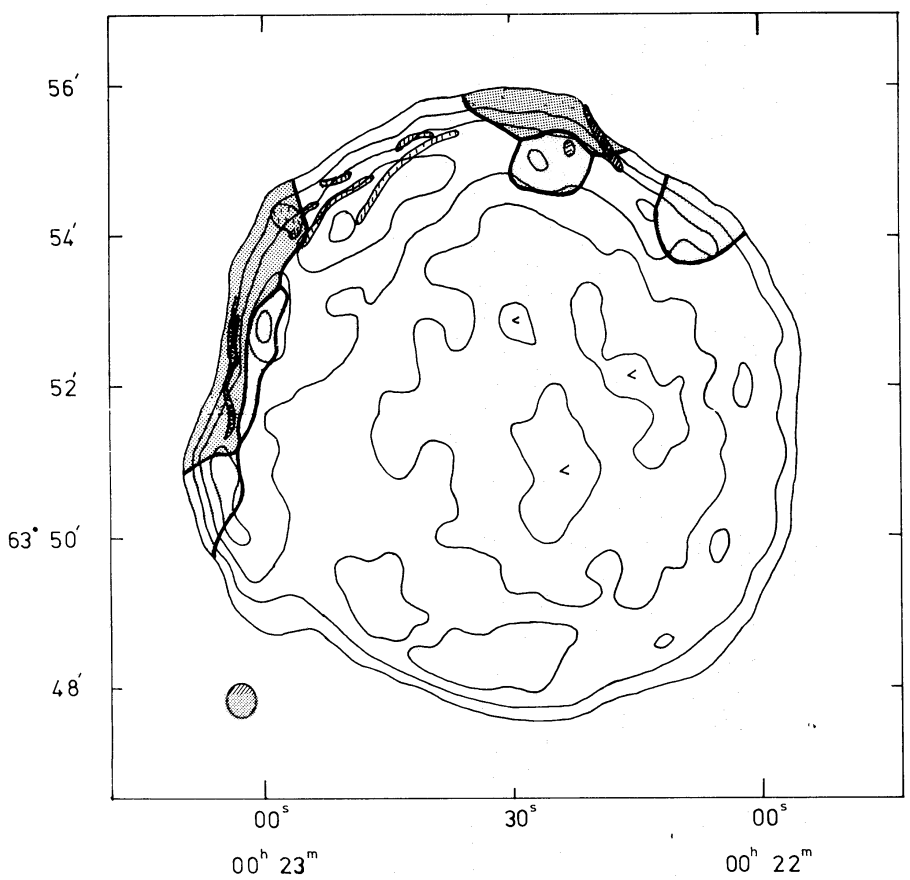

Figure 6. Superimposed on the 2.7-GHz map at 24 × 27 arcsec resolution are shown: (a) the optical filaments (shaded strips); (b) regions unpolarized (< 3 per cent) at 5 GHz (dark stippling); and regions depolarized between 5 and 1.4 GHz by a factor > 3 (light stippling).

is in the form of very thin sheets, comprising an approximately spherical surface around the remnant (van den Bergh, Marscher & Terzian 1973; Kirshner & Chevalier 1978). In the E and NW, the sheets are seen edge-on, and consequently appear as narrow and relatively bright filaments, the separation of which from the half-power contour of the radio edge (here unresolved, implying a sharp outer edge to the radio shell) is equal to the actual angular separation between the concentric surfaces defined by the optical sheets and the outer edge of the radio shell. Within the errors of measurement and alignment of the 12 arcsec resolution radio map with the optical features (by measurement of secondary reference star positions relative to the SAO standards), the two surfaces are found to be coincident (radial separation < 5 arcsec, i.e. < 2 per cent of the radius, or < 0.1 pc). The fact that all the other filaments are diffuse and appear to lie within the radio boundary is consistent with an interpretation of them as being also on the outer edge of the radio shell, but projected within the radio outline; since they are not orientated edge-on, the sheets are seen as diffuse patches. (Even here there is a tendency for the brightest parts to form linear features parallel to the outline of the radio remnant, presumably because of corrugations in the sheets caused by inhomogeneities in the interstellar medium.)

It is difficult to envisage that the very thin optical sheets can be defined by anything other than the shock front of the supernova remnant. Similarly the emissivity of the radio shell reaches a maximum at the unresolved outer edge (Fig. 8), and the extremely abrupt rise in emissivity here (by a factor > 10 in < 3 per cent of the radius of the remnant) also suggests that the outer edge of the radio shell coincides with the shock front. A contrary

conclusion was reached by Strom & Duin (1973) from radio polarization data, which seemed to indicate that the shock front lies some 0.4 pc outside the outer edge of the radio shell. The more sensitive polarization observations by Duin & Strom (1975) are analysed in the next section, however, and are shown to support a *coincidence* between the shock front and the unresolved edge of the radio shell.

The sheets of optical emission therefore represent a 'lighting-up' of the interstellar medium by the passage of the shock front; they are not permanent physical entities. The changes on a time-scale ~ 10 yr (van den Bergh *et al.* 1973) are then simply due to small-scale inhomogeneities in the swept-up medium. The proper motion of the optical filaments and hence, presumably, of the shock front, lies in the range 0.18–0.23 arcsec yr^{-1} (Kamper & van den Bergh 1978); the time-scale of variation thus implies either that the irregularities are typically no smaller than 2 arcsec (0.04 pc), or that the sheets have a thickness ~ 2 arcsec. This is consistent with their unresolved appearance and is close to the expected thickness (~ 1 arcsec) if the 'lighting-up' is due to the ionization of a partially neutral interstellar medium (Chevalier & Raymond 1978).

4.2 THE RADIO POLARIZATION

The radio polarization measurements on 3C 10 are summarized by Duin & Strom (1975). The intrinsic polarization of ≈ 10 per cent has its electric vectors aligned essentially tangentially, implying a radially ordered magnetic field. The average Faraday rotation measure over the source is $-249\ rad\ m^{-2}$, thought to arise in the interstellar medium between 3C 10 and the Sun, but observations at 1.4 GHz show that departures from the mean rotation occur in discrete 'cells' about 1 arcmin in size, within which the rotation is constant. These rotation cells are presumably discrete swept-up clouds, which Duin & Strom place in a 'Faraday screen' between the radio-emitting shell and the shock front. In this case there would be no depolarization of the radiation concomitant with the rotation of the plane of polarization. If, as argued above, the shock front coincides with the outer edge of the radio shell, these cells lie within the shell, and differential Faraday rotation within each cell will depolarize the radiation emitted at lower frequencies.

Duin & Strom find the rms deviation of the rotation measures of individual cells about the mean to be $16\ rad\ m^{-2}$. Using the formulae from Burn (1966), we find the intrinsic polarization to be reduced by a factor ≈ 0.75 at 1.4 GHz on the 'cells within shell' model. Since Strom & Duin (1973) find a typical polarization of 8 to 9 per cent in the centres of rotation cells at 1.4 GHz, an intrinsic polarization of ~ 11 per cent is expected.

The intrinsic polarization can in principle be obtained from observations at frequencies sufficiently high that depolarization is negligible. Pencil-beam results by Kundu & Velusamy (1971) at 10.7 GHz give a mean value of 8 per cent around the rim of the source, but this is essentially a lower limit as their comparatively large beam (3 arcmin) includes emission of lower fractional polarization from nearer the centre of the remnant. The aperture synthesis observations by Duin & Strom (1975) at 5 GHz suffer from an undersampled aperture plane, and hence reliable polarization values cannot be obtained. The authors estimate, however, that these are typically 10 per cent, rising to 16 per cent in places. These results do *not* rule out the 'cells within shell' model, despite Duin & Strom's assertion to the contrary.

Indeed, strong support *for* this model comes from the lower frequency (0.6 GHz) observations by Duin & Strom, in which no polarization stronger than 1 per cent was detected. This low value cannot be explained by beam-smearing between adjacent cells, as their beamwidth (1 arcmin) is smaller than many of the cells, and it is incompatible with their purely rotational 'Faraday screen' model. Differential Faraday rotation within a radio-emitting cell with a rotation measure of $16\ rad\ m^{-2}$ would, however, reduce its polarization

to ~ 1 per cent at this frequency. In addition, comparison of the 1.4-GHz (Strom & Duin 1973) and 5-GHz (Duin & Strom 1975) maps of polarized intensity reveals regions which are depolarized only at the lower frequency (as discussed further below); such depolarization is not possible on the 'Faraday screen' model. Hence, taken as a whole, the polarization data unambiguously favour a 'cells within shell' model rather than the 'Faraday screen', and are thus consistent with the shock front coinciding with the edge of the radio shell.

The regions where the radiation is depolarized at 1.4 GHz compared to 5 GHz are shown in Fig. 6, together with regions unpolarized at 5 GHz. The latter correlate strikingly well with the brightest optical filaments and with the two straight stretches of the remnant's outline (at the E and NW); the regions depolarized only at 1.4 GHz are contiguous to them. These facts can be simply explained if the blast wave is running into dense clouds in these two locations: the shock front is slowed, and hence is straightened; the higher emission measure produces the bright optical filaments; and the higher density of thermal electrons causes strong Faraday depolarization, large enough to depolarize at higher frequencies (5 GHz) towards the centre of the cloud, and only at lower frequencies (e.g. 1.4 GHz) towards its edge. These clouds are discussed further in Section 4.7.

4.3 MORPHOLOGY OF THE SHELL

Apart from the straight stretch in the E, the outline of the radio remnant can be well fitted by two circular arcs drawn from a common centre at $00^h\,22^m\,28^s.9$ ($\pm 0^s.7$), $+63°\,51'\,27''$ ($\pm 5''$). Two very faint stars lie near this position, but in such a crowded field the probability of a chance coincidence is high, and it cannot be assumed that either of them is the stellar remnant of the supernova. These arcs have radii of 257 ± 7 arcsec (NE) and 218 ± 7 arcsec (SW) (Fig. 7), corresponding to 5.0 and 4.2 pc. These two regions are also characterized by significantly different brightness temperatures, and by different scatters of rotation measures of the polarization cells about the mean (Table 2).

The average expansion velocity of the remnant is thus 18 ± 4 per cent higher towards the NE than towards the SW. This asymmetry could have arisen either from the interstellar density being lower to the NE of the supernova, or from an anisotropic initial explosion. In the former case, the goodness of the fits between the circular arcs and the shell implies that the supernova must have been close to the boundary in the interstellar medium across which the density changes by a factor ≈ 2 in less than 1 arcmin (≈ 1 pc). This interpretation is supported by the radio polarization data, which indicate that, while some parts of the NE section are currently encountering clouds with a very high density, the intercloud medium here is only about half as dense as the medium to the SW of the remnant (Section 4.6). The alternative explanation of an anisotropic explosion is difficult to reconcile with the abrupt discontinuity in the shock front at the SE, which would imply that the two shells of ejecta, differing in (kinetic energy/steradian) by a factor of 2, were here ejected in virtually the same direction. It seems more likely, therefore, that the asymmetry of 3C 10 is due to an abrupt change in interstellar density near the supernova. The SW and NE sectors will now be discussed separately.

4.4 RADIO EMISSION FROM THE SW SECTOR

The near-circularity of the outline of this sector, extending over more than 180°, suggests that it is spherically symmetric. The mean profile (Fig. 8) can thus be 'inverted' to yield the radial distribution of emissivity in the radio shell, although the inversion is complicated by the anisotropy of the synchrotron emission from each volume element of the shell, due to the predominantly radial alignment of the magnetic field.

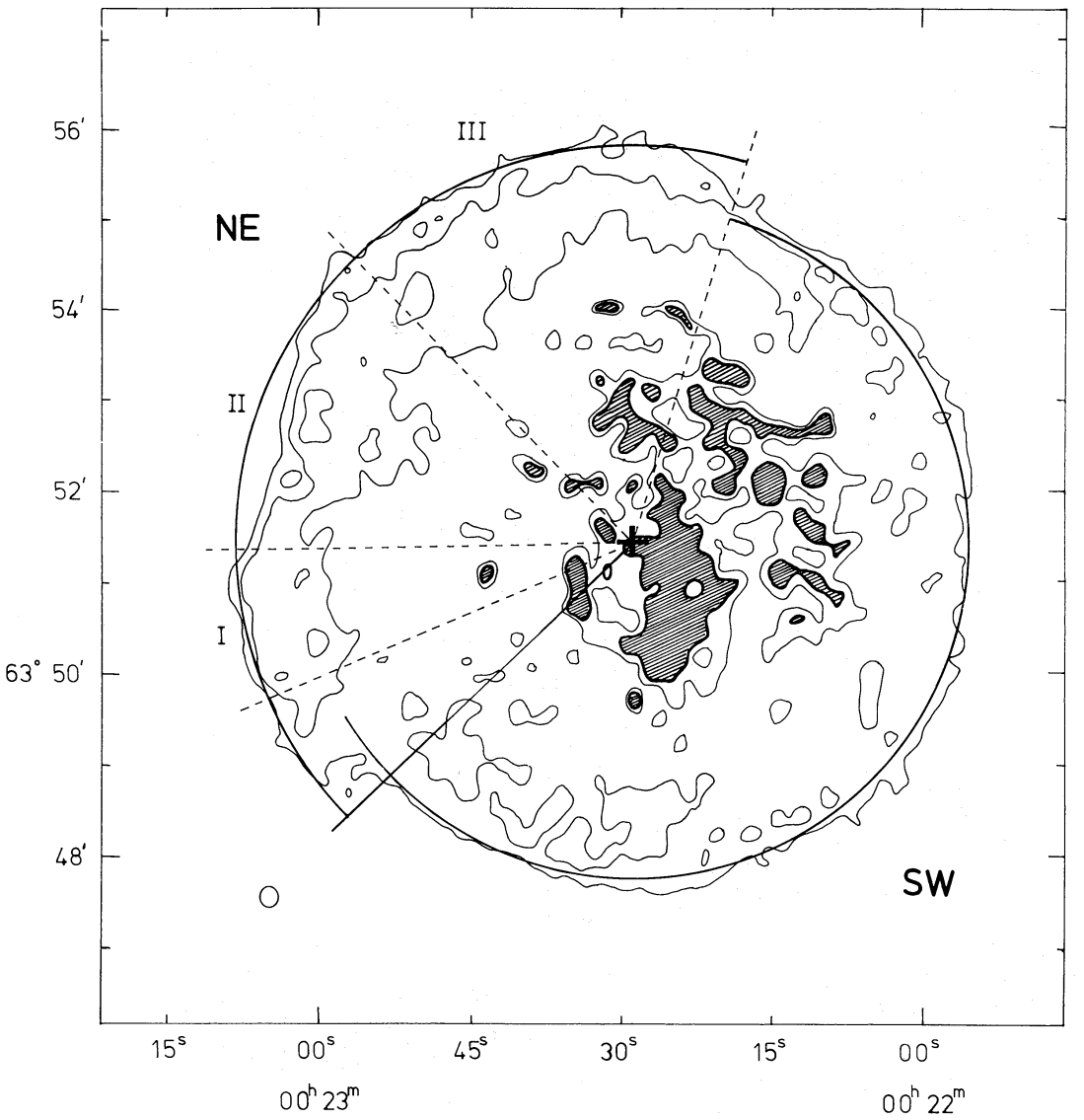

Figure 7. The two sectors of 3C 10, the heavy cross marking the mutual centre of the two arcs. The shading indicates regions where the observed intensity is less than half that of the model profile of Fig. 8; the beamshape is shown in the lower left corner.

Table 2. Properties of the two sectors of 3C 10.

	SW	NE
Radius of edge of radio shell (arcsec)	218 ± 7	257 ± 7
Mean brightness temperature at 2.7 GHz (K)	30 ± 3	43 ± 4
rms scatter in rotation measure (rad m^{-2})	20 ± 3	10 ± 2

The profile due to a uniform spherical shell is the weighted mean of the profiles for a shell containing a completely random field and that for a shell with a completely aligned field (Rosenberg 1970a, 1972), the proportions being dictated by the intrinsic polarization of ≈ 10 per cent (Duin & Strom 1975). A single shell of uniform emissivity does not give a

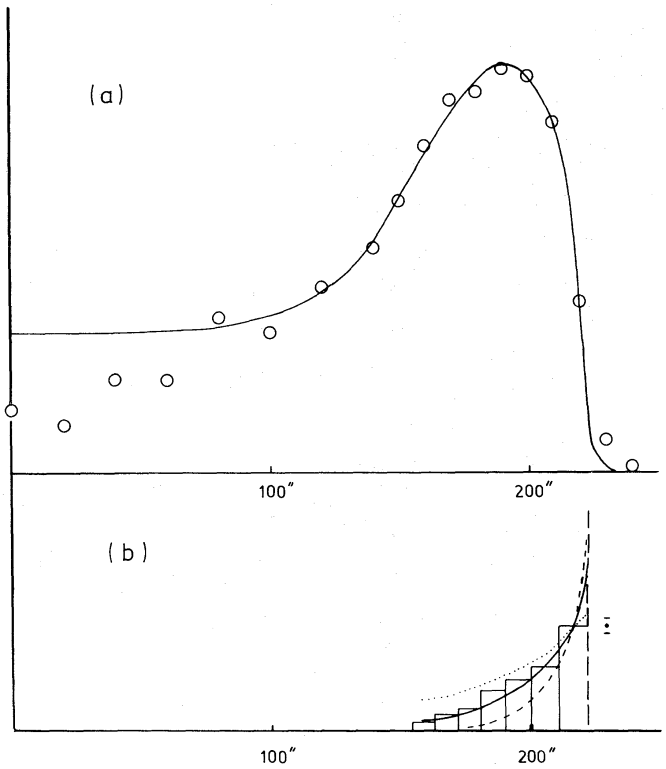

Figure 8. (a) The circles are the measured points for the mean radial profile of the SW sector, while the solid line is the profile derived by convolving the histogram (b) of emissivity with the telescope beam. The histogram shows the relative emissivities of cencentric subshells (each with thickness/outer radius = 0.05) required to fit the observed profile; the variation in each histogram allowed by the fitting procedure is shown by the error bar. Theoretical emissivity profiles (Section 4.4) are also shown. Dotted: $\epsilon \propto \rho_{\text{isothermal}}^{1.03}$ – isothermal with uniform n_r. Solid: $\epsilon \propto \rho_{\text{isothermal}}^{2.03}$ or $\epsilon \propto \rho_{\text{adiabatic}}^{1.03}$ (indistinguishable on this scale) – isothermal with $n_r \propto \rho_{\text{isothermal}}$, or adiabatic with n_r uniform. Dashed: $\epsilon \propto \rho_{\text{adiabatic}}^{2.03}$ – adiabatic with $n_r \propto \rho_{\text{adiabatic}}$.

good fit both to the width of the peak in the profile and to the steep outer edge, for any value of thickness to radius; the profile requires a shell whose emissivity increases towards the outer edge. To model the change in emissivity with radius, the shell has been divided into discrete subshells, each with (thickness/outer radius) = 0.05. The relative emissivity of these subshells has been adjusted until the total emission at each radius fits the observed radial profile of emission (Fig. 8).

The distribution of emissivity shown in the figure differs significantly from that derived by Strom & Duin (1973) for the following reasons:

(a) the resolution here is better by a factor ≈ 2;

(b) the NE sector, which has a different radius and is not spherically symmetric, has not been included in the measured profile; and

(c) the regions of enhanced emission within the remnant ('peaks' on the map) have not been removed before determining the profile, for reasons given in Section 3.1.

The histogram shown in Fig. 8 is thus believed to be a better representation of the distribution of emissivity in the shell of 3C 10.

It is evident from Fig. 8 that the central intensity of the remnant is considerably less than is predicted by the best-fitting model profile. The central brightness of a shell source is relatively insensitive to the exact distribution of emissivity in the shell, and is determined primarily by the ratio of aligned to random magnetic field. A shell whose radial magnetic

field is sufficient to produce the observed central deficit would give rise to an intrinsic polarization of ≈ 50 per cent, inconsistent with the observed ≈ 10 per cent. The region of anomalously low emission is also asymmetric with respect to the centre of the remnant (Fig. 7), implying that the discrepancy is not simply a function of radius.

A plausible explanation is that there is merely a region of low emissivity lying along the line of sight through the centre of the remnant. 'Breaks' are observed in the radio shells of the other known young supernova remnants: Cassiopeia A (Rosenberg 1970b), Kepler's supernova remnant (Gull 1975a) and the remnant of the supernova of AD 1006 (Milne 1971). A line of sight through one of these breaks would give a central deficiency of emission similar to that observed in 3C 10.

The emissivity profile of Fig. 8 requires a minimum energy of 1.4×10^{41} J, assuming that the radio spectrum extends only down to 10 MHz, that the only relativistic particles are electrons, and that the relativistic electrons are in equipartition with the magnetic field throughout the shell. Consideration of the dynamical evolution of young SNRs, however, allows a more detailed discussion of conditions within the radio-emitting shell.

The initial free expansion of the supernova ejecta is slowed as they 'sweep up' interstellar material. During this phase, the evolutionary state is conveniently parametrized by the *mass ratio* = (mass swept up)/(mass ejected). For a mass ratio < 1, there is a Rayleigh–Taylor instability at the interface of ejecta and swept-up matter, and turbulence is expected (Gull 1973a), powered by a reverse shock wave as the slower-moving ejecta catch up with the decelerated high-speed ejecta (McKee 1974; Gull 1975b). There is evidence for this in Cas A (Bell 1977), but in Tycho's SNR there is no evidence from either the optical or the radio observations for activity within the shock front, indicating that its mass ratio > 1, and the remnant has entered the second phase of evolution, when its properties are characterized by a self-similar blast wave.

The adiabatic self-similar solution (Sedov 1959) is usually adopted for young SNRs, but it can be questioned in that it predicts a very steep temperature gradient in the remnant, and the consequent heat conduction may have dynamical effects. The extreme case, that of an isothermal blast-wave, has been treated by Solinger, Rappaport & Buff (1975). Further complications arise from the fact that heat is conducted primarily by electrons, and in young SNRs the electron–ion energy-exchange time by Coulomb interactions ($\approx 10^3$ yr) is considerably longer than the age of the remnant. McKee (1974) has argued that collective plasma effects may be effective in equalizing electron and ion temperatures at the shock. If Coulomb interactions are the only *subsequent* means of energy exchange, the Sedov solution continues to be valid up to a remnant radius of ~ 26 pc (see Cowie 1977: with $E = 10^{44}$ J, $n_0 = 0.2$ cm^{-3} as determined in Section 4.5), when conditions approach the isothermal solution. The radius of the shock in 3C 10 (4.6 pc) and the density distribution behind it will thus be governed by the adiabatic solution unless non-Coulomb interactions are effective in keeping electron and ion temperatures similar throughout the shell.

The synchrotron emissivity (ϵ) is proportional to $n_r B^{1+\alpha}$ where n_r is the number density of relativistic electrons, B the magnetic field, and α the spectral index defined by $S_\nu \propto \nu^{-\alpha}$ (0.55 for 3C 10, Kellermann *et al.* 1969). The thermal plasma coincident with the radio shell in 3C 10 lies immediately behind the shock front and, for a remnant with mass ratio > 1, consists entirely of swept-up matter. Magnetic field 'frozen into' a plasma (density ρ) varies as $\rho^{2/3}$: hence

$$\epsilon \propto n_r \rho^{2(1+\alpha)/3} \propto n_r \rho^{1.03}.$$

The emissivity profile of 3C 10 can be interpreted on either type of self-similar solution (Fig. 8). On the adiabatic model, the profile is inconsistent with relativistic electron acceleration at the shock front, and requires a uniform distribution of electrons within the remnant.

These are presumably either supplied by a central stellar remnant, or remain from the earlier turbulent evolutionary phase (Gull 1973b; Chevalier, Robertson & Scott 1976). On the isothermal model, the profile requires that the relativistic electron density varies with the plasma density, and hence that particles are accelerated at the shock. A plausible mechanism for such acceleration has been proposed by Bell (1978), and if this is operating at the 3C 10 shock-front the present observations imply that the remnant is more closely following an isothermal than an adiabatic expansion.

On either model, energy arguments show that the interstellar magnetic field must undergo substantial amplification. In the case of adiabatic expansion, the mean interstellar magnetic field, B_0 (taken to be 0.25 nT; Manchester 1974), must be amplified by a factor of 4 in the tangential direction simply by passage through an adiabatic shock. The observed polarization of 3C 10, however, indicates that the radial component of the field is the stronger, some 25 per cent greater than the tangential field. The reason for this is not clear: natural 'field stretching' inherent in the Sedov solution (Duin & Strom 1975) produces a polarization in the correct sense only if the field is somehow randomized at the shock, which amounts to an amplification of the radial component by a factor of 4 *per se*, and even then it would produce a polarization of only 5 per cent for a radio shell lying just inside the shock front. Thus, despite 'field-stretching', the polarization data require a real amplification of the radial component by a factor of 5/4 over the compressional amplification of the tangential field, and it is possible that this mechanism can also amplify the tangential component above the nominal four times. Let us take the post-shock tangential field to be $4.0\beta B_0$. The total energy in relativistic electrons filling the remnant is then $2.3 \times 10^{42}\,\beta^{-3/2}$ J.

Supply from a central stellar remnant would required a mean power of $2 \times 10^{32}\beta^{-3/2}$ W. For comparison, the total power output of the Crab pulsar is $\sim 3 \times 10^{31}$ W, and 3C 10 shows no dynamical evidence for a central power source of this magnitude; in addition, optical and radio searches have failed to detect a pulsar (Reifenstein, Brundage & Staelin 1969; Nevo, Sadeh & Frohlich 1974). If the electrons are supplied by a central source with power $\ll 3 \times 10^{31}$ W, then $\beta \gg 7$. Alternatively, for acceleration at an earlier turbulent phase, a maximum $\approx$ ½ per cent of the initial kinetic energy of the supernova can be converted to relativistic electron energy (Gull 1973a). In the subsequent expansion, the energy of each electron is reduced by a factor of 0.7 by adiabatic losses. For a supernova of original energy 10^{44} J, a maximum of only 3×10^{41} J is thus available as relativistic electrons in a remnant like 3C 10. Extra amplification of the interstellar field is again required, with $\beta > 7$.

In the isothermal model, the tangential amplification of B_0 at the shock is only 2.3; if there is extra amplification of both components to increase this component to $2.3\,\beta B_0$, with the radial component 25 per cent greater, the total energy of the relativistic electrons is $4.5 \times 10^{42}\,\beta^{-3/2}$ J. Without extra amplification if the field ($\beta = 1$), the energy density of the relativistic electrons immediately behind the shock would be 10^4 times higher than the magnetic energy density; this seems unlikely. Equipartition of energy between field and electrons at the shock requires $\beta \approx 14$. The rate of decrease of the magnetic field behind an isothermal shock is such that the radio-emitting shell is then approximately in equipartition throughout, and the total energy in relativistic electrons plus magnetic field is just the minimum energy of 1.4×10^{41} J.

4.5 EXTERNAL DENSITY TO THE SW

The cells in the SW sector have an rms scatter about the mean of 20 rad m^{-2} (from Fig. 7 of Duin & Strom 1975). An estimate of the interstellar density around the SW edge of the remnant can be derived from the following simple model. Assume a constant external

number density, n_0, and that the rotation cells are distinguished by different strengths and directions for the magnetic field. The rms value of the field in the cells *before* they are swept up is taken to be 0.25 nT.

Taking into account the compression of the magnetic field at the shock, possible extra amplification by a factor β, and the density and magnetic field profiles behind the shock, the value of $n_0\beta$ is 1.9 cm^{-3} (adiabatic) or 3.0 cm^{-3} (isothermal). From the energy arguments of the last section, $\beta > 7$ (adiabatic) or ≈ 14 (isothermal), giving $n_0 < 0.3$ cm^{-3} and $n_0 \approx 0.2$ cm^{-3} respectively.

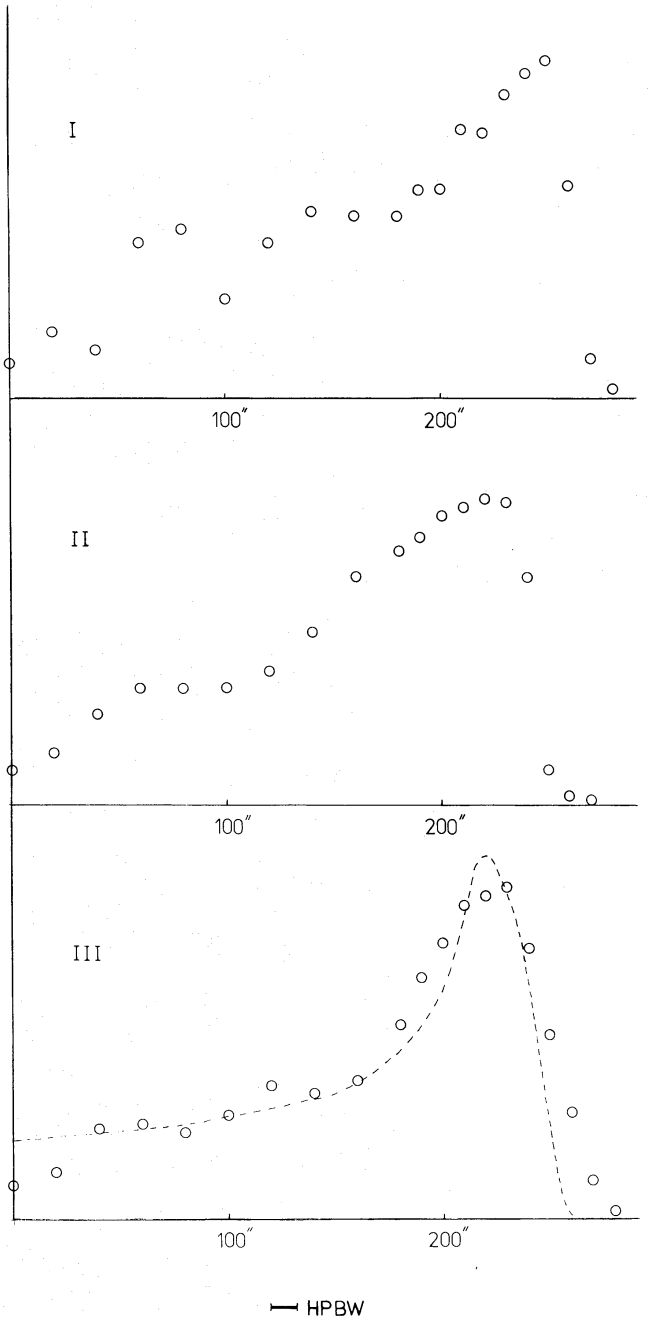

Figure 9. Mean profiles for the three regions of the NE sector indicated in Fig. 7. In sector II the profile at radii > 140 arcsec has been measured along the chords in position angle 165°, parallel to the straight edge of the remnant here. The edge of the source is unresolved in both this sector and sector I with the 12-arcsec beam. The dashed curve superimposed on the data for sector III is the theoretical emission from a uniform shell with thickness/outer radius = 0.15, convolved with the telescope beam.

A lower limit on n_0 follows from a consideration of the mass swept up by the remnant. For the SW sector this is $7.5\, n_0\, (\Omega_{SW}/4\pi) M_\odot$, where Ω_{SW} is the solid angle subtended by this sector at the centre of the remnant. For a typical ejected mass of $\approx 1\, M_\odot$ for a type I supernova (Gordon 1975), the mass ejected into this sector is $\sim (\Omega_{SW}/4\pi) M_\odot$; the present mass ratio of 3C 10 (> 1) thus requires $n_0 > 0.13\,\mathrm{cm}^{-3}$. These limits imply an external number density in the SW of $0.2 \pm 0.1\,\mathrm{cm}^{-3}$ (on either expansion model), a mass ratio between 1 and 2.5, and an extra amplification of the magnetic field at the shock by a factor of 7–14 (adiabatic) or ~ 14 (isothermal).

4.6 THE NE SECTOR

This sector is so distorted by interaction with dense clouds that its emissivity profile cannot be determined; mean intensity profiles are, however, shown in Fig. 9. The rms scatter of rotation measure about the mean is $10\,\mathrm{rad\,m}^{-2}$ (from Fig. 7 of Duin & Strom 1975), when the 'cloud' regions are omitted. The mean interstellar density is thus about half that to the SW of the remnant. For an isotropic supernova explosion which has now reached the self-similar phase, the NE radius should then be 15 per cent larger than the SW radius, in good agreement with the observed value of 18 ± 4 per cent (Section 4.3).

4.7 THE DENSE CLOUDS

The NE section is encountering at least two dense clouds. A lower limit to the density of the E and NW clouds follows from the depolarization of 5-GHz radiation (Fig. 6), which requires a rotation measure $> 700\,\mathrm{rad\,m}^{-2}$. Allowing for the different geometry, the density in these clouds $> 8\times$ that of the SW sector, if the magnetic field strengths are similar. The synchrotron brightness temperature in the NE is 40 per cent higher than in the SW, implying

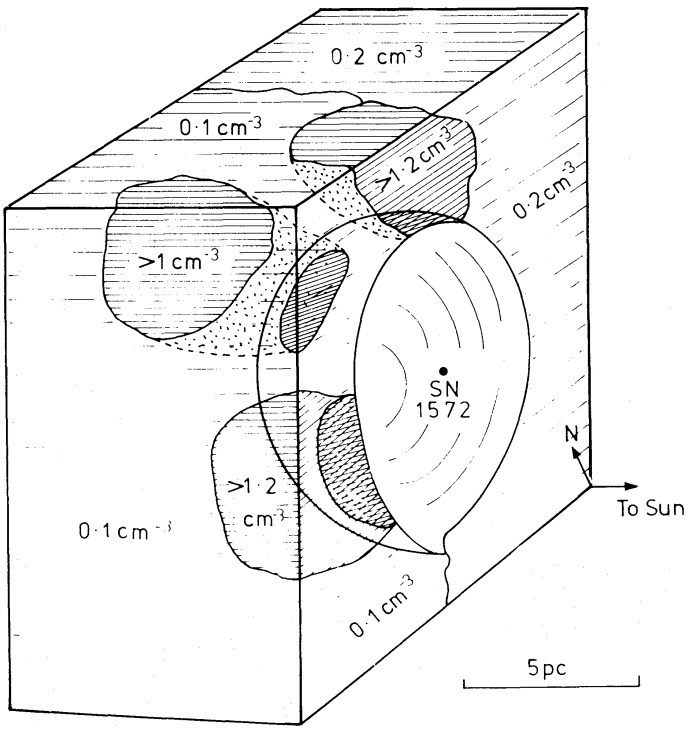

Figure 10. The structure of the interstellar medium in the vicinity of Tycho's SNR, as derived in Sections 4.5, 4.6 and 4.7.

a magnetic field 20 per cent greater, and a density ratio > 6. Hence the density of the clouds is $> 1.2\,\mathrm{cm}^{-3}$.

The optically emitting sheets in the NE (seen superimposed on the radio shell) are almost as bright as the short filament in the NW, suggesting a third cloud with a comparable density. Since the radio emission here would be depolarized at frequencies below 5 GHz, the NE of 3C 10 should have a lower average polarization than the SW (even when the depolarized regions associated with the E and NW clouds are omitted); Duin & Strom (1973) have indeed found such an effect at 1.4 GHz. The cloud must lie on the far side of the remnant; if it were on the near side it would cause very large Faraday rotation of the radiation from the far side, an effect which is not observed.

The resulting picture of the interstellar medium in the vicinity of 3C 10 is shown in Fig. 10. Structure on four different scales can be distinguished: (a) a medium in the SW, uniform over > 10 pc, and separated from a similar region of lower density to the NE by a boundary < 1 pc thick; (b) clouds ~ 5 pc in extent and at least an order of magnitude denser than the surrounding medium; (c) 'cells' ~ 1 pc across, distinguished by different magnetic-field configurations; and (d) density fluctuations on a scale < 0.04 pc which cause the variation in optical appearance of the filaments in the E. This analysis suggests that the detailed investigation of SNR structure can be a useful probe of local conditions in the interstellar medium.

Acknowledgments

My thanks to all members of MRAO involved in the OMT observations; to Noel Argue for assistance in measuring the optical positions; to Peter Scheuer and John Shakeshaft for comments on the manuscript; and particularly to Steve Gull for many interesting and useful discussions on supernova remnants. Financial support from the Northern Ireland Department of Education during the initial stages of this work is gratefully acknowledged; I also thank Heather Couper for subsequent intellectual support.

References

Baade, W., 1945. *Astrophys. J.*, **102**, 309.
Baldwin, J. E., 1967. *Radio Astronomy and the Galactic System* (IAU Symp. 31), ed. van Woerden, H., Academic Press, London, p. 337.
Bell, A. R., 1977. *Mon. Not. R. astr. Soc.*, **179**, 573.
Bell, A. R., 1978. *Mon. Not. R. astr. Soc.*, **182**, 443.
Branch, D., 1977. *Mon. Not. R. astr. Soc.*, **179**, 401.
Burn, B. J., 1966. *Mon. Not. R. astr. Soc.*, **133**, 67.
Caswell, J. L. & Lerche, I., 1979a. *Mon. Not. R. astr. Soc.*, **187**, 201.
Caswell, J. L. & Lerche, I., 1979b. *Aust. J. Phys.*, **32**, 79.
Chevalier, R. A. & Raymond, J. C., 1978. *Astrophys. J.*, **225**, L27.
Chevalier, R. A., Robertson, J. W. & Scott, J. S., 1976. *Astrophys. J.*, **207**, 450.
Cowie, L. L., 1977. *Astrophys. J.*, **215**, 226.
Dickel, J. R., 1969. *Astrophys. Lett.*, **4**, 109.
Duin, R. M. & Strom, R. G., 1975. *Astr. Astrophys.*, **39**, 33.
Elsmore, B., Kenderdine, S. & Ryle, M., 1966. *Mon. Not. R. astr. Soc.*, **134**, 87.
Emerson, D. I., Klein, U. & Haslam, C. G. T., 1979. *Astr. Astrophys.*, **76**, 92.
Gordon, C., 1975. *Astrophys. J.*, **198**, 765.
Goss, W. M., Schwarz, U. J. & Wesselius, P. R., 1973. *Astr. Astrophys.*, **28**, 305.
Gull, S. F., 1973a. *Mon. Not. R. astr. Soc.*, **161**, 47.
Gull, S. F., 1973b. *Mon. Not. R. astr. Soc.*, **162**, 135.

Gull, S. F., 1975a. *Mon. Not. R. astr. Soc.*, **171**, 237.
Gull, S. F., 1975b. *Mon. Not. R. astr. Soc.*, **171**, 263.
Hermann, B. R. & Dickel, J. R., 1973. *Astr. J.*, 78, 879.
Kamper, K. W. & van den Bergh, S., 1978. *Astrophys. J.*, **224**, 851.
Kellermann, K. I., Pauliny-Toth, I. I. K. & Williams, P. J. S., 1969. *Astrophys. J.*, **157**, 1.
Kirshner, R. P. & Chevalier, R. A., 1978. *Astr. Astrophys.*, **67**, 267.
Klein, U., Emerson, D. T., Haslam, C. G. T. & Salter, C. J., 1979. *Astr. Astrophys.*, **76**, 120.
Kundu, M. R. & Velusamy, T., 1971. *Astrophys. J.*, **163**, 231.
McKee, C. F., 1974. *Astrophys. J.*, **188**, 335.
Manchester, R. N., 1974. *Astrophys. J.*, **188**, 637.
Mebold, U. & Hills, D. L., 1975. *Astr. Astrophys.*, **42**, 187.
Milne, D. K., 1971. *Aust. J. Phys.*, **24**, 757.
Milne, D. K., 1979. *Aust. J. Phys.*, **32**, 83.
Nevo, I., Sadeh, D. & Frohlich, A., 1974. *Astr. Astrophys.*, **36**, 311.
Reifenstein, E. C. III., Brundage, W. D. & Staelin, D. H., 1969. *Astrophys. J.*, **156**, L125.
Rosenberg, I., 1970a. *Mon. Not. R. astr. Soc.*, **147**, 215.
Rosenberg, I., 1970b. *Mon. Not. R. astr. Soc.*, **151**, 109.
Rosenberg, I., 1972. *PhD thesis*, University of Cambridge.
Sedov, L. I., 1959. *Similarity and Dimensional Methods in Mechanics*, Academic Press, New York.
Solinger, A., Rappaport, S. & Buff, J., 1975. *Astrophys. J.*, **201**, 381.
Strom, R. G. & Duin, R. M., 1973. *Astr. Astrophys.*, **25**, 351.
van den Bergh, S., Marscher, A. P. & Terzian, Y., 1973. *Astrophys. J. Suppl.*, **26**, 19.
Verschuur, G. L., 1973. *Astr. Astrophys.*, **24**, 193.
Weiler, K. W. & Seielstad, G. A., 1971. *Astrophys. J.*, **163**, 455.
Williams, D. R. W., 1973. *Astr. Astrophys.*, **28**, 309.

Appendix

The distance to 3C 10 is still uncertain. One method of determining it is the surface brightness–diameter relation. The recent modification of this by Caswell & Lerche (1979a, b), to take account of the variation of density of the interstellar medium with distance from the galactic plane, has improved the fit for other young type I SNRs, and Milne (1979) gives 5.0 kpc as the distance of 3C 10.

Another method is to derive the kinematic distance from H I absorption. Absorption extends to a velocity of at least $-70\,\mathrm{km\,s^{-1}}$, corresponding to a distance > 6 kpc on the Schmidt rotation model for the Galaxy at a galactic longitude of 120° (Williams 1973; Goss, Schwarz & Wesselius 1973); but before this distance is accepted uncritically – especially in view of its conflict with the limit derived below – we may note that the absorption spectrum becomes very weak beyond $-49\,\mathrm{km\,s^{-1}}$, corresponding to 4.0 kpc (see the spectrum in Williams 1973). The weak absorption at the more extreme velocity can be accounted for in at least two ways: (a) the well-known anomalous velocity field in the Perseus arm present at galactic longitudes 105–137° (Verschuur 1973); (b) a disturbance in the H I velocity field related to 3C 10 itself: the H I absorption spectrum of the young SNR Cas A shows a similar weak, extreme-velocity feature caused by the remnant (Mebold & Hills 1975).

An upper limit to the distance of 3C 10 can be deduced from its origin in a type I supernova (Baade 1945); these supernovae have an initial photospheric expansion velocity of $10\,900 \pm 700\,\mathrm{km\,s^{-1}}$ (Branch 1977). If (a) all the ejecta travel at this velocity, and (b) no interstellar medium is swept up, the distance to the remnant immediately follows from this velocity, the remnant's known age (400 yr at epoch of the present observations) and its measured mean angular radius (475 ± 10 arcsec), by the classical method of expansion parallax. The result is 4.2 ± 0.3 kpc. The effect of the swept-up interstellar medium is twofold: it initially increases the size of the remnant by forming a shell around the ejecta; but

by slowing the expansion it causes the remnant to become progressively smaller than the radius predicted on linear expansion. For a mass ratio $\geqslant 1$, the distance is $\leqslant 4.3$ kpc (2σ upper limit). If a significant fraction of the ejecta travels more slowly than the photospheric velocity, this limit is further reduced.

These results are only consistent if the distance is close to 4.0 kpc, and this value is adopted here.